Science AAAS

www.sciencemag.org/content/345/6202/1317/suppl/DC1

Supplementary Materials for

# Chaotic dynamics of stellar spin in binaries and the production of misaligned hot Jupiters

Natalia I. Storch, Kassandra R. Anderson, Dong Lai*

*Corresponding author. E-mail: dong@astro.cornell.edu

Published 12 September 2014, *Science* **345**, 1317 (2014)
DOI: 10.1126/science.1254358

**This PDF file includes:**

Materials and Methods

Supplementary Text

Figs. S1 to S7

## S1 Materials and Methods

For the "pure" Kozai problem discussed in the earlier part of the main text, we integrate the standard quadrupole Kozai-Lidov equations for the planet's orbital elements (assuming $M_p \ll M_\star, M_b$). These are given by

$$\begin{aligned}
\frac{de}{dt} &= t_{\mathrm{k}}^{-1} \frac{15}{8} e\sqrt{1-e^2} \sin 2\omega \sin^2 \theta_{\mathrm{lb}}, \\
\frac{d\Omega}{dt} &= t_{\mathrm{k}}^{-1} \frac{3}{4} \frac{\cos\theta_{\mathrm{lb}} \left(5e^2 \cos^2 \omega - 4e^2 - 1\right)}{\sqrt{1-e^2}}, \\
\frac{d\theta_{\mathrm{lb}}}{dt} &= -t_{\mathrm{k}}^{-1} \frac{15}{16} \frac{e^2 \sin 2\omega \sin 2\theta_{\mathrm{lb}}}{\sqrt{1-e^2}}, \\
\frac{d\omega}{dt} &= t_{\mathrm{k}}^{-1} \frac{3\left[2(1-e^2) + 5\sin^2\omega(e^2 - \sin^2\theta_{\mathrm{lb}})\right]}{4\sqrt{1-e^2}},
\end{aligned} \tag{S1}$$

where $e$ is the planet's orbital eccentricity, $\theta_{\mathrm{lb}}$ is the angle between the planet orbital angular momentum axis and the binary axis $\hat{\mathbf{L}}_b$, $\Omega$ is the longitude of the ascending node, $\omega$ is the argument of periastron, and $t_{\mathrm{k}}^{-1}$ is the characteristic Kozai rate, given by Eq. (1) of the main text. We choose the binary orbital plane to be the invariant plane. In all the cases we consider, we take as our initial condition $\Omega_0 = 0$ and $\omega_0 = 0$ (thus, $\omega$ always circulates rather than librates; see Fig. S2). Note, however, that this is not a particularly special choice, since for the initial inclinations $\theta_{\mathrm{lb}}$ we consider ($85^\circ - 89^\circ$) the maximum eccentricity is the same for the circulating and librating cases, and the rates of precession of the node ($\Omega_{\mathrm{pl}}$, Eq. 2) are only slightly different.

We evolve the precession of the stellar spin according to the equation

$$\frac{d\hat{\mathbf{S}}}{dt} = \Omega_{\mathrm{ps}} \hat{\mathbf{L}} \times \hat{\mathbf{S}}, \tag{S2}$$

where $\Omega_{\mathrm{ps}}$ is given by Eq. (4), and $\hat{\mathbf{L}} = (\sin\theta_{\mathrm{lb}} \sin\Omega, -\sin\theta_{\mathrm{lb}}\cos\Omega, \cos\theta_{\mathrm{lb}})$ in the inertial frame where the $z$-axis is parallel to the binary axis $\hat{\mathbf{L}}_b$.

In the latter part of the main text, we add short-range forces to our system. We use the expressions given in *(19)* for periastron advances due to General Relativity, planet spin-induced quadrupole, and static tide in the planet. We also add nodal and apsidal precession of the planetary orbit due to the spin-induced stellar quadrupole. This introduces the following terms to the orbital evolution equations:

$$
\begin{aligned}
\frac{d\omega}{dt} &= \omega_\star \left(1 - \frac{3}{2}\sin^2\theta_{\rm sl} - \frac{\cos\theta_{\rm lb}}{\sin\theta_{\rm lb}}\cos\theta_{\rm sl}\frac{\partial\cos\theta_{\rm sl}}{\partial\theta_{\rm lb}}\right), \\
\frac{d\Omega}{dt} &= \omega_\star \frac{\cos\theta_{\rm sl}}{\sin\theta_{\rm lb}}\frac{\partial\cos\theta_{\rm sl}}{\partial\theta_{\rm lb}}, \\
\frac{d\theta_{\rm lb}}{dt} &= -\omega_\star \frac{\cos\theta_{\rm sl}}{\sin\theta_{\rm lb}}\frac{\partial\cos\theta_{\rm sl}}{\partial\Omega},
\end{aligned}
\tag{S3}
$$

where

$$
\begin{aligned}
\cos\theta_{\rm sl} &= \hat{\mathbf{L}}\cdot\hat{\mathbf{S}} = S_x\sin\theta_{\rm lb}\sin\Omega - S_y\sin\theta_{\rm lb}\cos\Omega + S_z\cos\theta_{\rm lb}, \\
\frac{\partial\cos\theta_{\rm sl}}{\partial\theta_{\rm lb}} &= S_x\cos\theta_{\rm lb}\sin\Omega - S_y\cos\theta_{\rm lb}\cos\Omega - S_z\sin\theta_{\rm lb}, \\
\frac{\partial\cos\theta_{\rm sl}}{\partial\Omega} &= S_x\sin\theta_{\rm lb}\cos\Omega + S_y\sin\theta_{\rm lb}\sin\Omega,
\end{aligned}
\tag{S4}
$$

and $\omega_\star = -\Omega_{\rm ps}S/(L\cos\theta_{\rm sl})$.

Finally, we add tidal dissipation in the planet to our equations. We use the standard weak friction tidal dissipation model *(41,42)*:

$$
\frac{1}{a}\frac{da}{dt} = \frac{1}{t_a}\frac{1}{(1-e^2)^{15/2}}\left[(1-e^2)^{3/2}f_2(e)\frac{\Omega_{\rm s,p}}{n} - f_1(e)\right], \tag{S5}
$$

$$
\frac{1}{e}\frac{de}{dt} = \frac{11}{4}\frac{1}{t_a}\frac{1}{(1-e^2)^{13/2}}\left[(1-e^2)^{3/2}f_4(e)\frac{\Omega_{\rm s,p}}{n} - \frac{18}{11}f_3(e)\right], \tag{S6}
$$

where $a$ is the semi-major axis, $\Omega_{\rm s,p}$ is the spin rate of the planet, the functions $f_1 - f_4$ are defined as

$$
\begin{aligned}
f_1(e) &= 1 + \frac{31}{2}e^2 + \frac{255}{8}e^4 + \frac{185}{16}e^6 + \frac{25}{64}e^8, \\
f_2(e) &= 1 + \frac{15}{2}e^2 + \frac{45}{8}e^4 + \frac{5}{16}e^6, \\
f_3(e) &= 1 + \frac{15}{4}e^2 + \frac{15}{8}e^4 + \frac{5}{64}e^6, \\
f_4(e) &= 1 + \frac{3}{2}e^2 + \frac{1}{8}e^4,
\end{aligned}
\tag{S7}
$$

(S8)

and $t_a$ is a characteristic timescale, given by

$$\frac{1}{t_a} = 6k_2 \Delta t_{\rm L} \left(\frac{M_\star}{M_p}\right) \left(\frac{R_p}{a}\right)^5 n^2, \tag{S9}$$

where $n$ is the mean motion of the planet, $k_2$ is the tidal Love number and $\Delta t_{\rm L}$ is the tidal lag time. For Jupiter, $k_2 = 0.37$ and we take $\Delta t_{\rm L} = 0.1$ s (corresponding to $k_2/Q \approx 10^{-5}$ at a tidal forcing period of $6.5$ hours). We therefore use $\Delta t_{\rm L} = 0.1\chi$ s, where $\chi$ is a tidal enhancement factor, which we take to be $14$ for Fig. 5 (left) and $1400$ for Fig. 5 (right), in order to ensure that the planets in our test cases circularize within the lifetime of their host stars. For all the sample cases considered in this work, we assume the planet spin to be pseudosynchronous with the orbit, i.e. $\Omega_{\rm s,p}/n = f_2(e)/[(1-e^2)^{3/2} f_5(e)]$, with $f_5(e) = 1 + 3e^2 + (3/8)e^4$. Relaxing this assumption does not qualitatively change our results. (For pseudosynchronous spin, the periastron advance due to planet's rotation bulge is always smaller than that due to tidal distortion.)

Equivalent evolution equations for the spin-triple system can be found in *(21,26)*.

# S2 Supplementary Text

## S2.1 Figures

In this section we provide several supplementary figures that facilitate deeper understanding of the rich dynamics exhibited by the stellar spin during Kozai cycles and migration.

As stated in the main text, the division between different regimes of stellar spin behavior depends on the planet semi-major axis, binary semi-major axis, and the product of planet mass and stellar spin frequency. In Fig. S1, we illustrate these divisions in the $a_b - a$ space for several different values of $\hat{M}_p \equiv (\hat{\Omega}_\star/0.05)(M_p/M_J)$. We note that for real systems, short-range effects due to General Relativity (GR) and tidal/rotation distortion of the planet may affect the Kozai cycles. For the parameter space explored in this paper, the GR effect dominates. When the Kozai precession frequency $\dot{\omega}_{\rm k} \sim t_{\rm k}^{-1}(1-e^2)^{3/2}$ becomes comparable to the GR-induced precession frequency $\dot{\omega}_{\rm GR}$, the Kozai cycle is arrested. In this case, the maximum eccentricity achieved during a Kozai cycle is reduced, and any planet undergoing Kozai cycles in will fail to become a hot Jupiter if $r_p = a(1 - e_{\max})$ is larger than $\sim 0.1$ AU. Thus, the effect of GR can restrict the available parameter space in which adiabatic evolution (regime III) happens *and* a hot Jupiter is created. However, the presence of short-range forces and tidal dissipation also alters the topology of the chaos in the parameter space, making it difficult to draw a direct connection between the regime divisions in the "pure" Kozai system and the results of our dissipative simulations. In fact, the results of Fig. 5 (left) demonstrate that, indeed, it is possible for hot Jupiters to experience adiabatic evolution.

In order to explore the three regimes of stellar spin evolution, we create surfaces of section (Fig. 2) by sampling the spin trajectory every time the orbital trajectory comes back to the same region of phase space. In Fig. S2 we show the orbital trajectory in phase space, with and without short-range forces, and mark the point at which we choose to sample the spin evolution.

In the main text, we demonstrate that in the "transadiabatic" regime (regime II), stellar spin has the potential to undergo both chaotic motion and regular quasiperiodic motion, depending on the parameters of the system. In Fig. 1 we present an example of a chaotic trajectory. Here, in Fig. S3 we present an example of a periodic transadiabatic trajectory: even at late times, the "real" and "shadow" trajectories match perfectly.

Finally, in Fig. S4 we present a sample time evolution for the Kozai problem with added short-range forces, tidal dissipation and stellar spindown, showing how the final semi-major axis $a_{\mathrm{f}}$ and spin-orbit misalignment angle $\theta_{\mathrm{sl}}^{\mathrm{f}}$ are attained. Each point in Fig. 5 represents the result of such evolution.

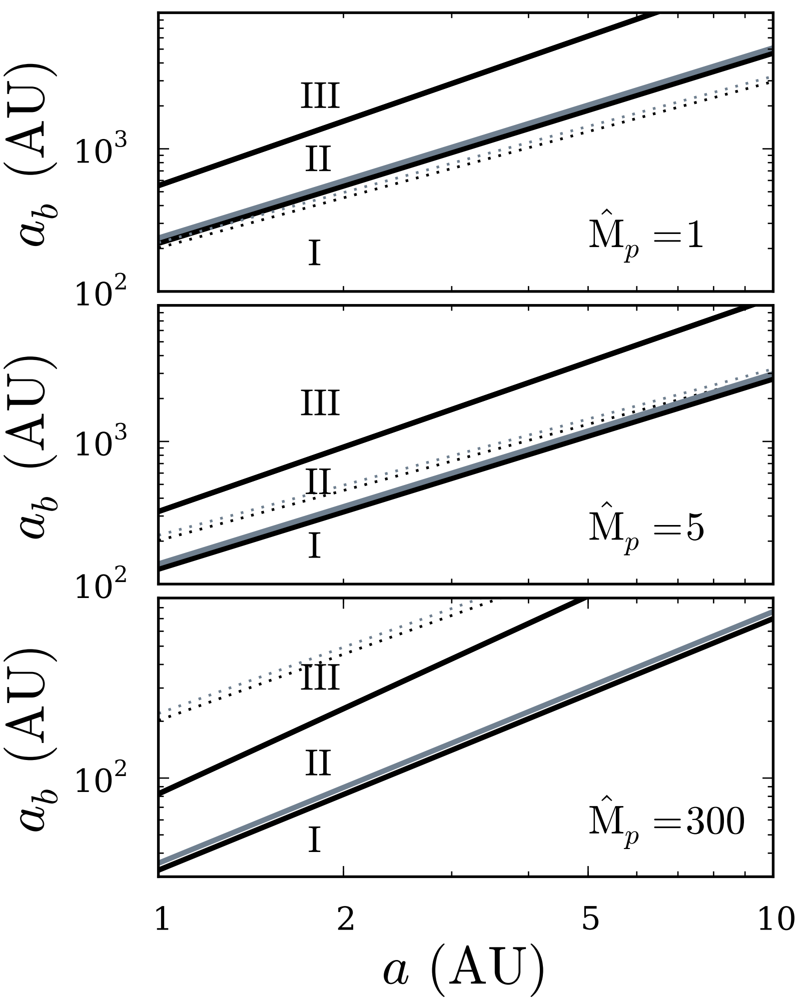


Figure S1: Breakdown of parameter space into the three regimes of spin evolution, as discussed in the text. *Black*: for a periastron distance of $r_p = a(1 - e_{\rm max}) = 0.03$ AU; *gray*: for $r_p = 0.05$ AU. Here $\hat{M}_p = (\hat{\Omega}_\star/0.05)(M_p/M_J)$. The regimes are determined by the relative values of the stellar spin precession frequency $\Omega_{\rm ps}$ and the nodal precession frequency $\Omega_{\rm pl}$ of the planet's orbit. Note that $\Omega_{\rm ps}$ depends on $\cos\theta_{\rm sl}$, and for concreteness we use $\cos\theta_{\rm sl} = 1$. $\Omega_{\rm pl}$ is a complicated function of eccentricity and $\theta_{\rm lb}$ (Eq. 2), which we approximate as $\Omega_{\rm pl} \approx -t_{\rm k}^{-1}/(1 - e^2)$ in making this figure. The lines separating Regimes I and II are given by $|\Omega_{\rm ps,max}| \approx 0.5|\Omega_{\rm pl,max}|$, where $\Omega_{\rm ps,max}$ and $\Omega_{\rm pl,max}$ are equal to $\Omega_{\rm ps}$ and $\Omega_{\rm pl}$ evaluated at $(1 - e_{\rm max}) = r_p/a$. The line separating Regimes II and III is given by $|\Omega_{\rm ps,0}| \approx 2|\Omega_{\rm pl,0}|$, where $\Omega_{\rm ps,0}$, $\Omega_{\rm pl,0}$ are equal to $\Omega_{\rm ps}$ and $\Omega_{\rm pl}$ evaluated at $e = 0$. The dotted lines mark the boundary at which the effect of GR becomes significant, approximated by $\dot{\omega}_{\rm GR} \approx t_{\rm k}^{-1}(1 - e_{\rm max}^2)^{-1/2}$. Above the dotted lines, GR will suppress the Kozai cycles, so that the system cannot reach the specified $r_p$. In Regimes I and III the spin precession frequency never overlaps with the nodal precession frequency, and the spin evolution is expected to be regular and periodic. In Regime II, the two frequencies are equal for some value of $e$ during the Kozai cycle, and therefore secular spin-orbit resonance develops, potentially leading to chaos. Note that the parameters shown in the lowest panel ( $\hat{M}_p = 300$) correspond to a low-mass star rather than a planet.

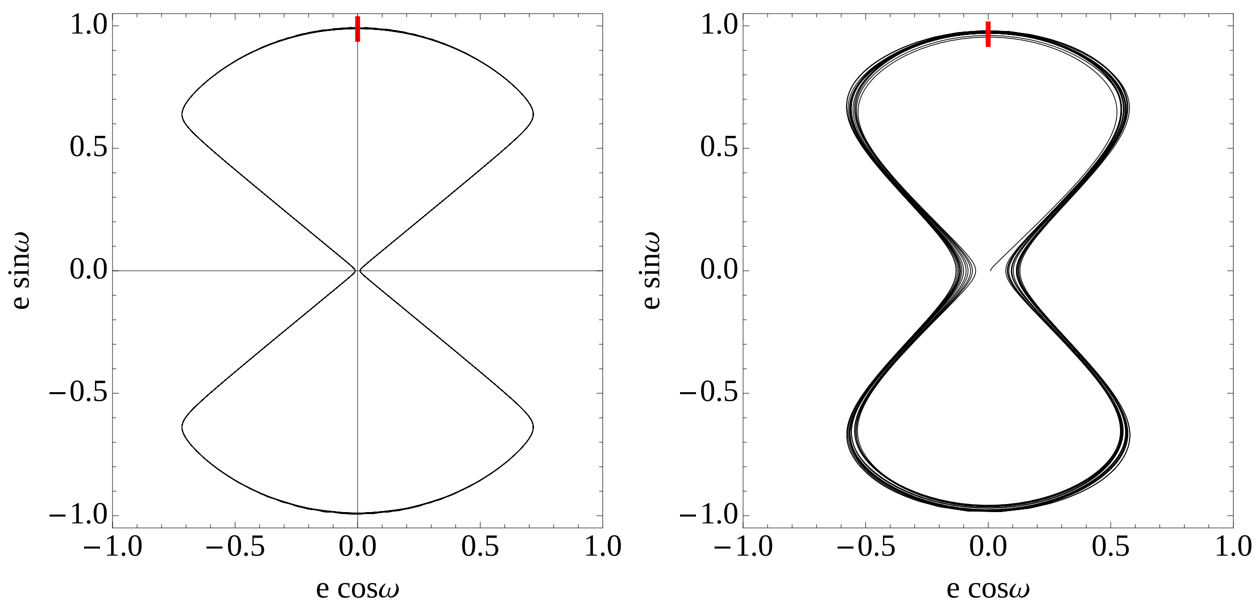


Figure S2: Orbital trajectory in $e - \omega$ phase space, for the "pure" Kozai problem (left), and with the addition of short-range forces (right). $\omega$ circulates with a period that is twice the period of the eccentricity oscillations. In red, we mark the point in the trajectory where we choose to sample the spin evolution in generating Figs. 2 and 4: i.e., every time the trajectory passes that point, we record the stellar spin orientation.

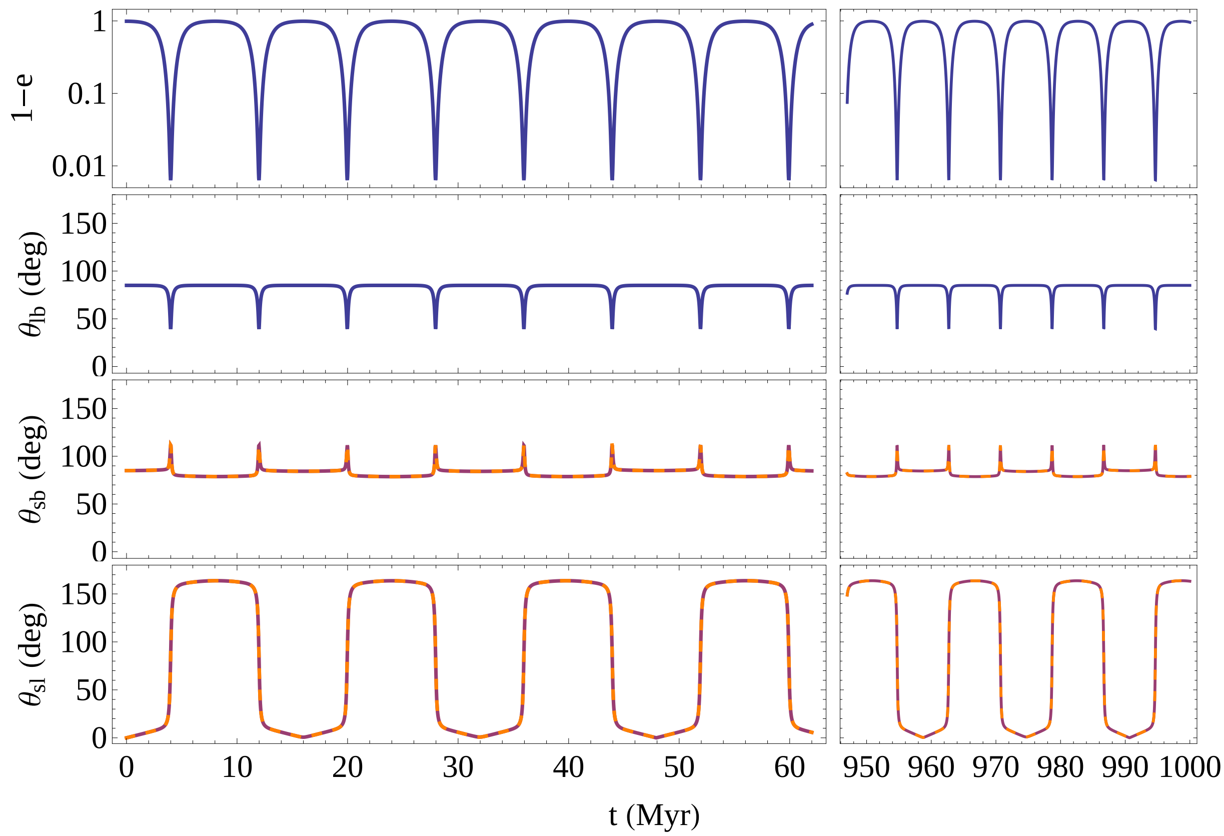


Figure S3: Sample evolution curves for a trajectory in a periodic island of regime II, demonstrating how the stellar spin evolves through many Kozai cycles. We plot a "real" trajectory (red solid lines) and a "shadow" trajectory (orange dashed lines), used to evaluate the degree of chaotic behavior. The trajectories are initialized such that the "real" starts with $\hat{\mathbf{S}}$ parallel to $\hat{\mathbf{L}}$, and the "shadow" with $\hat{\mathbf{S}}$ misaligned by $10^{-6}\mathrm{deg}$ with respect to $\hat{\mathbf{L}}$. The parameters are $a = 1$AU, $a_b = 200$AU, $e_0 = 0.01$, $\theta_{\rm lb}^0 = 85°$, $\hat{\Omega}_\star = 0.03$, $M_p = 1.025 M_J$. This figure corresponds to the red points of Fig. 2 (bottom left) and the red curve of Fig. 3 (left). It is perfectly periodic: even at late times, the "real" and "shadow" trajectories match perfectly.

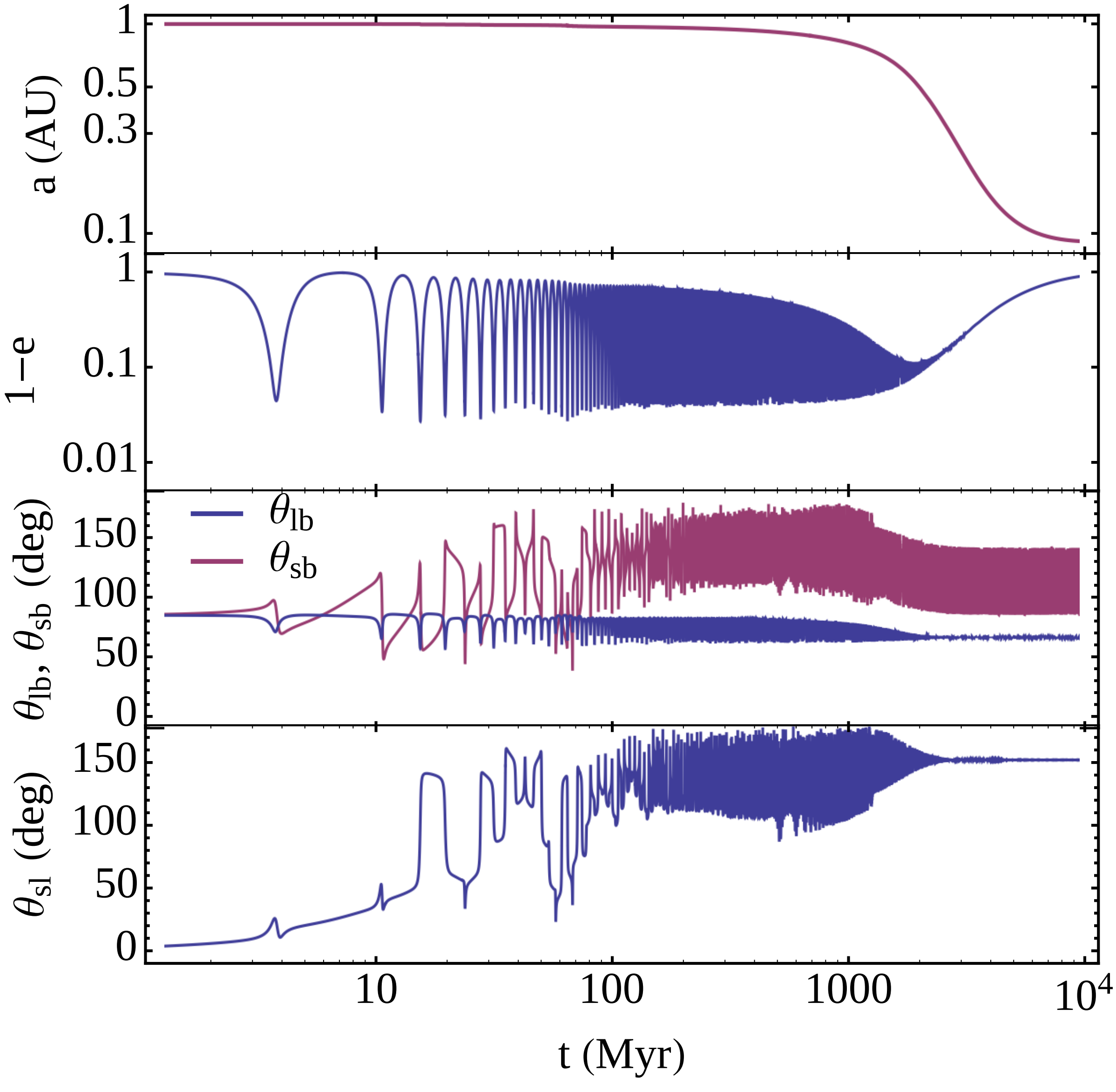


Figure S4: Sample orbital and spin evolution, including tidal dissipation and stellar spindown. The parameters for this run are $a_0 = 1$AU, $a_b = 200$AU, $e_0 = 0.01$, $\theta^0_{\rm lb} = 85°$, $\hat{\Omega}_{\star,0} = 0.05$, $M_p = 5M_J$, $\chi = 700$.

## S2.2 Toy Model

We consider a toy model in order to gain a better understanding of the dynamical behavior of the "real" Kozai system with stellar spin evolution (i.e. the system on which we focused in the main text). In this model, the stellar spin axis $\hat{\mathbf{S}}$ satisfies Eq. (S2), and the orbital axis $\hat{\mathbf{L}}$ evolves according to

$$\frac{d\hat{\mathbf{L}}}{dt} = \Omega_{\rm pl}\hat{\mathbf{L}}_b \times \hat{\mathbf{L}}, \tag{S10}$$

where we have neglected the back-reaction torque of the stellar spin on the planetary orbit (this back-reaction can be included but it does not introduce qualitatively new features when $L \gg S$), and the nutation of the orbital angular momentum vector $\hat{\mathbf{L}}$. The external binary axis $\hat{\mathbf{L}}_b$ is fixed in time, and the angle between $\hat{\mathbf{L}}$ and $\hat{\mathbf{L}}_b$ is constant. The spin precession rate $\Omega_{\rm ps}$ is a function of eccentricity (and time) [see Eq. (4)]. In the case of pure Kozai oscillations (i.e. without extra precession effects), the eccentricity is a periodic function of time, varying between $0$ and $e_{\rm max}$. We imitate this oscillatory behavior by adopting the following explicit form for $\Omega_{\rm ps}$:

$$\Omega_{\rm ps}(t) = \Omega_{\rm ps,0} f(t) \cos\theta_{\rm sl}, \quad \text{with } \ f(t) \equiv \frac{1+\varepsilon}{1+\varepsilon\cos\Omega_0 t}, \tag{S11}$$

where $\Omega_0$ represents the Kozai oscillation frequency. The precession frequency of $\hat{\mathbf{L}}$ around $\hat{\mathbf{L}}_b$ has the approximate eccentricity dependence $\Omega_{\rm pl} \propto [2(1-e^2)^{-1} - 1]$ in the real system, and therefore in our toy model takes the form

$$\Omega_{\rm pl} = \Omega_{\rm pl,0}(2f^{2/3} - 1), \qquad \text{where} \qquad \Omega_{\rm pl,0} = \frac{3}{4}\Omega_0 \cos\theta_{\rm lb}. \tag{S12}$$

During a Kozai cycle, $\Omega_{\rm ps}$ varies from $\Omega_{\rm ps,0}\cos\theta_{\rm sl}$ to $\Omega_{\rm ps,max} = \Omega_{\rm ps,0}(1+\varepsilon)\cos\theta_{\rm sl}/(1-\varepsilon)$. We adopt $\varepsilon = 0.99$ in our examples below. Thus, the parameter $\omega_{\rm ps,0} \equiv \Omega_{\rm ps,0}/\Omega_{\rm pl,0}$ determines whether the system is nonadiabatic ($\omega_{\rm ps,0} \lesssim 0.1$), transadiabatic ($0.1 \lesssim \omega_{\rm ps,0} \lesssim 1$), or fully adiabatic ($\omega_{\rm ps,0} \gtrsim 1$).

For a given $\Omega_{\rm ps,0}$, we numerically integrate Eqs. (S2) and (S10) for 1000 "Kozai cycles," record the values of $\theta_{\rm sl}$ and $\theta_{\rm sb}$ at eccentricity maxima (i.e., $\Omega_0 t = \pi, 3\pi, 5\pi, \cdots$), and then plot these values in the $\theta_{\rm sl} - \omega_{\rm ps,0}$ and $\theta_{\rm sb} - \omega_{\rm ps,0}$ planes. We repeat the process for different values of $\omega_{\rm ps,0}$. The results are shown in Fig. S5 for initial $\theta_{\rm lb} = 60^\circ$ (and initial $\theta_{\rm sl} = 0^\circ$). The range of $\omega_{\rm ps,0}$ has been chosen to illustrate the nonadiabatic, transadiabatic and fully adiabatic regimes.

As in the real system, our toy model exhibits periodic/quasiperiodic solutions and chaotic zones, and the level of chaos is determined by the parameter $\omega_{\rm ps,0}$. If we use the spreads of $\theta_{\rm sl}$ and $\theta_{\rm sb}$ as a measure of chaos, we see that the system generally becomes more chaotic with increasing $\omega_{\rm ps,0}$, until $\omega_{\rm ps,0}$ reaches $\sim 5$, beyond which the system becomes fully-adiabatic ($\theta_{\rm sl} \to 0$ and $\theta_{\rm sb}$ approaches a constant). However, multiple periodic islands exist in the ocean of chaos. Figure S6 illustrates the time evolution of $\theta_{\rm sl}$ and $\theta_{\rm sb}$ in several of these periodic islands, along with an example of chaotic evolution. Figure S7 compares $\delta(t) = |\hat{\mathbf{S}}_{\rm real}(t) - \hat{\mathbf{S}}_{\rm shadow}(t)|$ (where the shadow trajectory has an initial condition nearly identical to the real one) for the different cases, clearly showing the difference between the periodic islands and chaotic evolution.

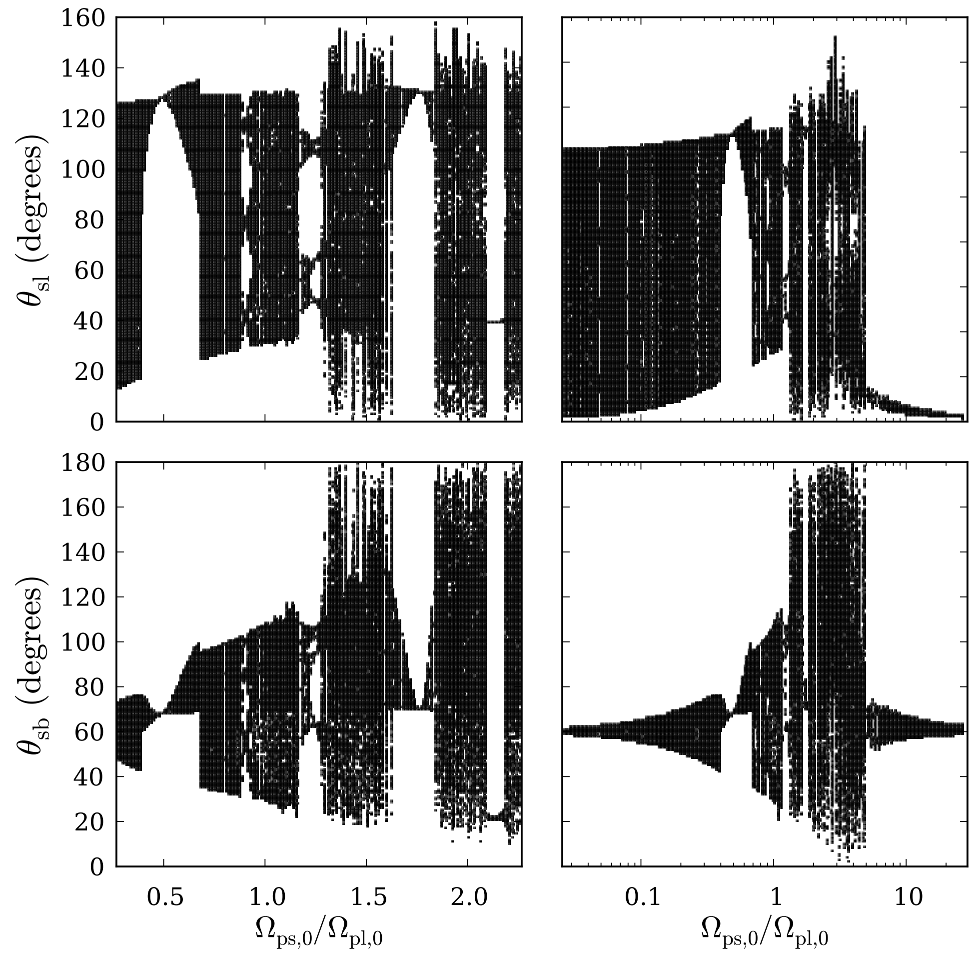


Figure S5: Angles $\theta_{\rm sl}$ and $\theta_{\rm sb}$ evaluated at maximum eccentricity (where $\Omega_0 t = \pi, 3\pi, 5\pi...$ for 1000 cycles) as functions of $\omega_{\rm ps,0} \equiv \Omega_{\rm ps,0}/\Omega_{\rm pl,0}$. The initial angle between $\hat{\mathbf{L}}$ and $\hat{\mathbf{L}}_b$ is $\theta^0_{\rm lb} = 60°$, and $\hat{\mathbf{S}}$ and $\hat{\mathbf{L}}$ are initially aligned. The range of $\omega_{\rm ps,0}$ (on the logarithmic scale) in the right panels is chosen to illustrate the behavior of the three regimes (nonadiabatic, transadiabatic, and fully adiabatic). The narrow range of $\omega_{\rm ps,0}$ (on the linear scale) in the left panels exhibits the existence of periodic and quasiperiodic islands within the (chaotic) transadiabatic zones.

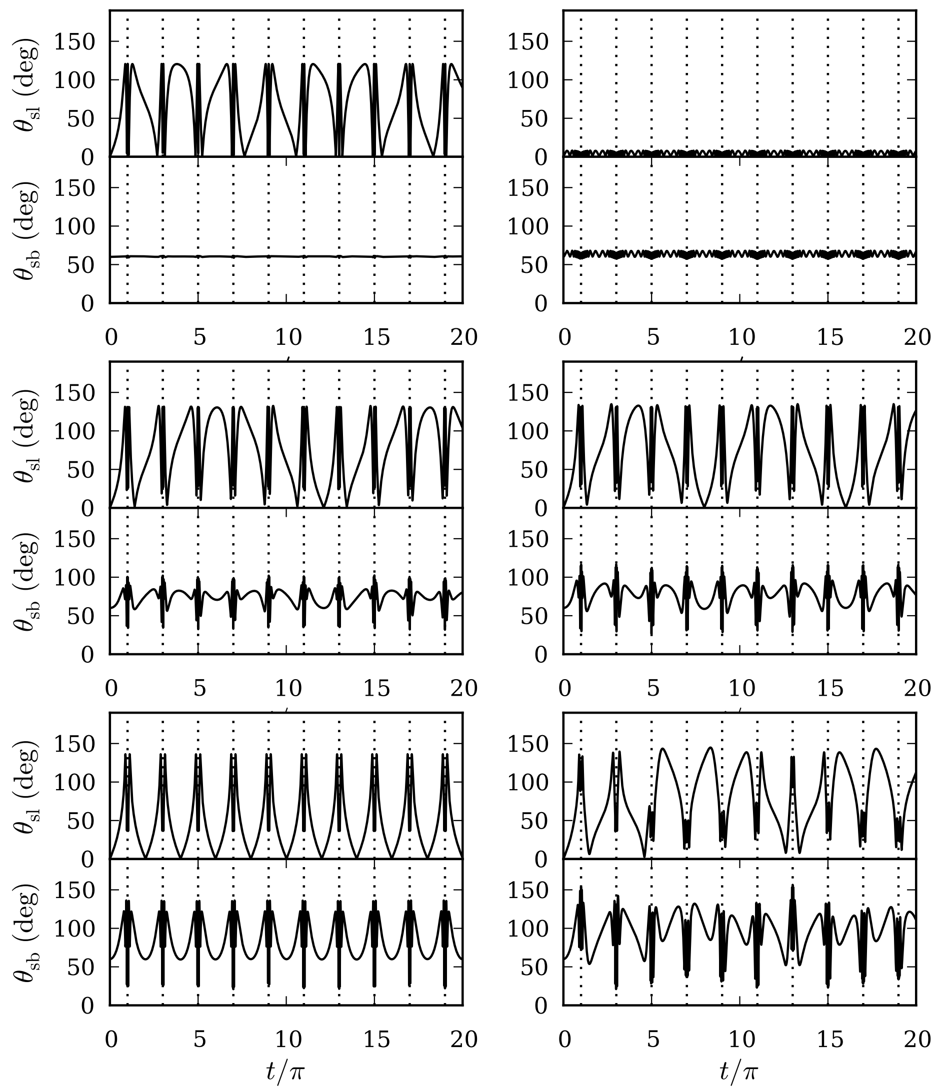


Figure S6: Angles $\theta_{\rm sl}$ and $\theta_{\rm sb}$ as functions of time, demonstrating the various behaviors of different orbits shown in Figure S5, including the three distinct regimes, and the difference between periodic and chaotic evolution in the transadiabatic regime. Time is in units of $\Omega_0 = 1$ (Eq. S11), and has been scaled by $\pi$. The dashed lines, included for reference, are located at odd-integers (when the system is at maximum eccentricity). *Upper left panel*: $\omega_{\rm ps,0} \equiv \Omega_{\rm ps,0}/\Omega_{\rm pl,0} = 0.023$, nonadiabatic, so that $\theta_{\rm sb} \approx$ constant. *Upper right panel*: $\omega_{\rm ps,0} = 13.3$, fully adiabatic, so that $\theta_{\rm sl} \approx \theta_{\rm sl}^0 \approx 0$. *Middle left panel*: $\omega_{\rm ps,0} = 0.89$, transadiabatic but periodic, with period$= 12\pi$. *Middle right panel*: $\omega_{\rm ps,0} = 1.25$, transadiabatic but periodic, with period$= 16\pi$. *Bottom left panel*: $\omega_{\rm ps,0} = 2.13$, transadiabatic but periodic, with period$= 2\pi$. *Bottom right panel*: $\omega_{\rm ps,0} = 2.35$, transadiabatic, with no discernible periodic behavior, chosen to illustrate chaotic evolution. See also Fig. S7 for further comparison between periodic and chaotic evolution.

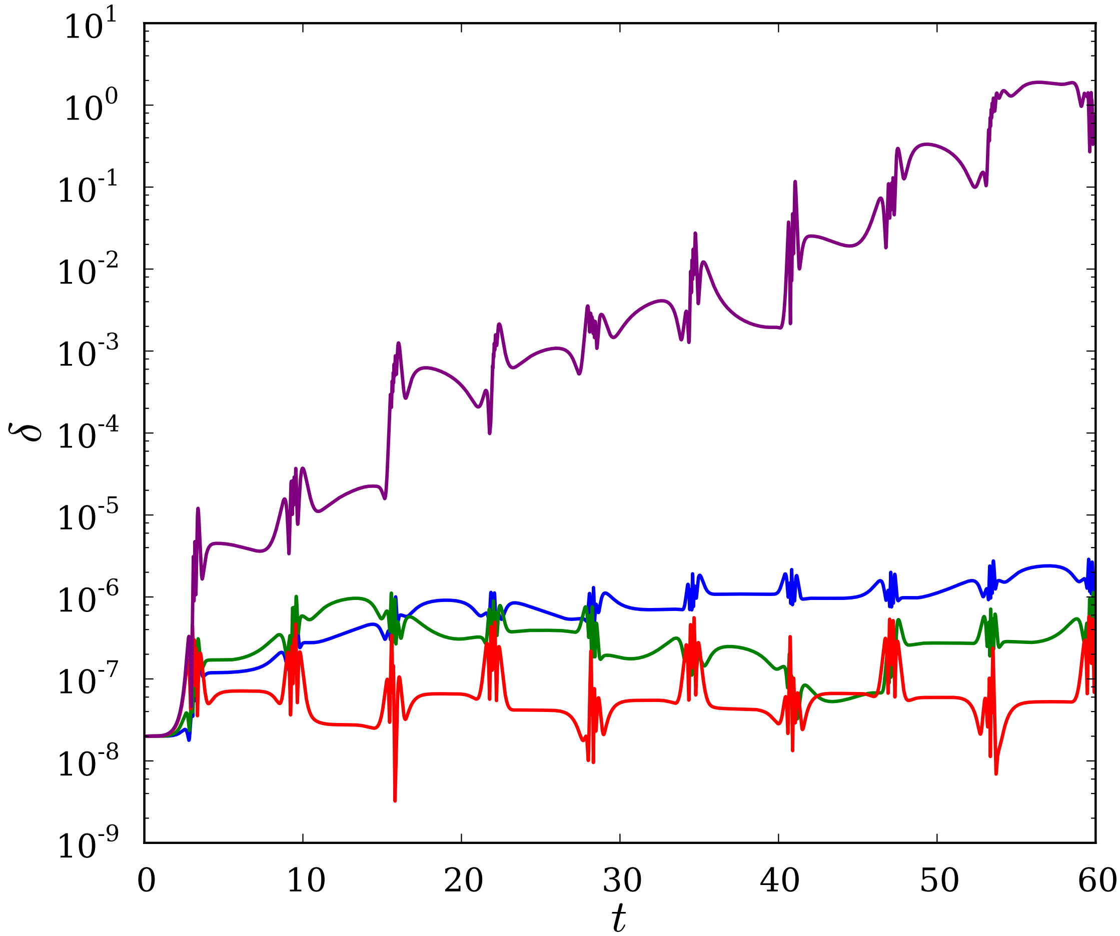


Figure S7: Difference ($\delta$) in the spin vector $\hat{\mathbf{S}}$ between "real" and "shadow" trajectories for the four transadiabatic systems shown in Fig. S6 (bottom 4 panels), starting with an initial $\delta_0 = 10^{-8}$. Time is in units of $\Omega_0 = 1$. Three examples of periodic evolution are shown, where $\omega_{\rm ps,0} \equiv \Omega_{\rm ps,0}/\Omega_{\rm pl,0} = 0.89$ (blue), $\omega_{\rm ps,0} = 1.25$ (green), $\omega_{\rm ps,0} = 2.13$ (red), as well as a chaotic example $\omega_{\rm ps,0} = 2.35$ (purple). Compare with Figure S6. For the periodic examples $\delta$ remains small, while in the chaotic example, $\delta$ increases exponentially, and eventually saturates to its maximum value of $\delta = 2$.